

# Shedding Light on Three-Body Recombination in an Ultracold Atomic Gas

A. Härter<sup>1</sup>, A. Krüchow<sup>1</sup>, M. Deiß<sup>1</sup>, B. Drews<sup>1</sup>, E. Tiemann<sup>2</sup>, & J. Hecker Denschlag<sup>1</sup>

<sup>1</sup>Institut für Quantenmaterie and Center for Integrated Quantum Science and Technology IQ<sup>ST</sup>, Universität Ulm, 89069 Ulm, Germany

<sup>2</sup>Institut für Quantenoptik, Leibniz Universität Hannover, 30167 Hannover, Germany

Three-body recombination is a prime example of the fundamental interaction between three particles. Due to the complexity of this process it has resisted a comprehensive description. Experimental investigations have mainly focussed on the observation of corresponding loss rates without revealing information on the reaction products. Here, we provide the first general experimental study on the population distribution of molecular quantum states after three-body recombination in a non-resonant regime. We have developed a highly sensitive detection scheme which combines photoionization of the molecules with subsequent ion trapping. By analyzing the ionization spectrum, we identify the population of energy levels with binding energies up to  $h \times 750$  GHz. We find a broad population of electronic and nuclear spin states and determine a range of populated vibrational and rotational states. The method presented here can be expanded to provide a full survey of the products of the recombination process. This may be pivotal in developing an in-depth model that can qualitatively and quantitatively predict the reaction products of three-body recombination.

While cold collisions of two atoms are understood to an excellent degree, the addition of a third collision partner drastically complicates the interaction dynamics. In the context of Bose-Einstein condensation in atomic gases, three-body recombination plays a crucial role<sup>1-4</sup> and it constitutes a current frontier of few-body physics<sup>5-7</sup>. However, the investigations focussed mainly on the atom loss rates established by the recombination events. Discussions of the final states populated in the recombination process were restricted to the special case of large two-body scattering lengths<sup>8,9</sup> and culminated in the prediction and observation of Efimov resonances<sup>10-12</sup>. In the limit of large scattering lengths, recombination has been seen to predominantly yield molecules in the most weakly bound states<sup>13,14</sup>. However, in the more general case of a scattering length comparable to the van der Waals radius, the recombination products might depend on details of the interaction potential. In fact, ongoing theoretical studies using simplified models indicate that recombination does not necessarily always favor the most weakly bound state<sup>15</sup> (see also<sup>16</sup>). In general, recombination processes are of fundamental interest in various physical systems<sup>1,17,18</sup>. The control and tunability of ultracold atomic systems provide an experimental testbed for a detailed understanding of the nature of these processes.

Here, we demonstrate the probing of molecules with binding energies up to  $h \times 750$  GHz (where  $h$  is Planck's constant) generated via three-body recombination of ultracold thermal <sup>87</sup>Rb atoms. We produce the atomic sample in an optical dipole trap located within a linear Paul trap. The recombination and detection process is illustrated in Fig. 1a-d. Following a recombination event, the created Rb<sub>2</sub> molecule can undergo resonance-enhanced multi-photon ionization (REMPI) by absorbing photons from the dipole trap laser at a wavelength around 1064.5nm. The ion is then captured in the Paul trap and detected essentially background-free with very high sensitivity on the single particle level. Fig. 1e shows a simplified scheme of the Rb<sub>2</sub> and Rb<sub>2</sub><sup>+</sup> potential energy curves. From weakly-bound molecular states three photons suffice to reach the molecular ionization threshold. An additional photon may dissociate the molecular ion. By scanning the frequency of the dipole trap laser by more than 60 GHz we obtained a high resolution spectrum featuring more than 100 resonance peaks. This dense and

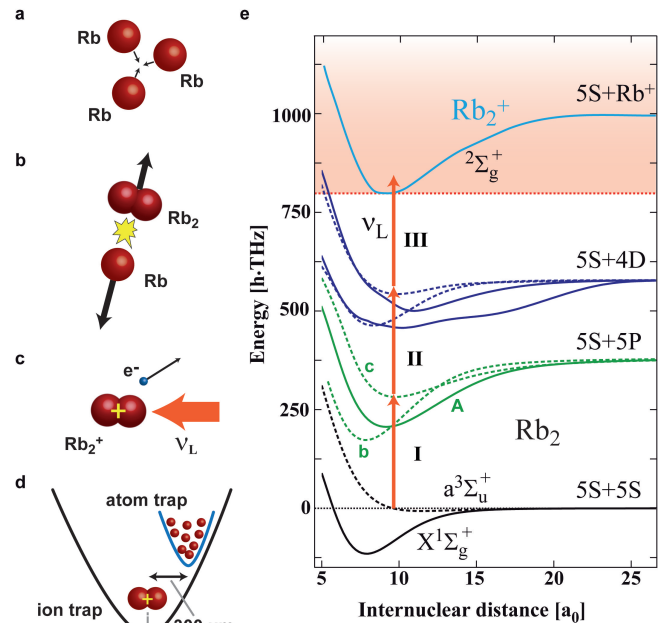


**Figure 1 | Illustration of recombination and ionization in the atom-ion trap.** a, A three-body collision in the ultracold gas of <sup>87</sup>Rb atoms leads to a recombination event in which, b, a Rb<sub>2</sub> molecule is formed with high kinetic energy. c, While the atom is lost from the trap, the molecule can be photoionized in a REMPI process and trapped in the Paul trap. d, The relative positions of the atom and ion trap centers are shifted by about 300 μm to avoid atom-ion collisions. e, Potential energy curves of the Rb<sub>2</sub> and Rb<sub>2</sub><sup>+</sup> molecule adapted from refs<sup>19,20</sup>. The curves A, b, c, are A<sup>1</sup>Σ<sub>u</sub><sup>+</sup>, b<sup>3</sup>Π<sub>u</sub>, c<sup>3</sup>Σ<sub>u</sub><sup>+</sup>. The internuclear distance is given in units of Bohr radii a<sub>0</sub>. A REMPI path with three photons is shown. It can create Rb<sub>2</sub><sup>+</sup> ions in vibrational states up to  $v \approx 17$ .

complex spectrum contains information which vibrational, rotational and hyperfine levels of the  $\text{Rb}_2$  molecule are populated. We present an analysis of these data and make a first assignment of the most prominent resonances. This assignment indicates that in the recombination events a broad range of levels is populated in terms of vibrational, rotational, electronic and nuclear spin quantum numbers.

Our experimental scheme to detect cold molecules makes use of the generally excellent detection efficiencies attainable for trapped ions. It is related to proven techniques where cold molecules in magneto-optical traps were photoionized from the singlet and triplet ground states<sup>19,21–25</sup> (see also ref<sup>26</sup>). Our method is novel as it introduces the usage of a hybrid atom-ion trap which significantly improves the detection sensitivity. We perform the following experimental sequence. A thermal atomic sample typically containing  $N_{\text{at}} \approx 5 \times 10^5$  spin-polarized  $^{87}\text{Rb}$  atoms in the  $|F = 1, m_F = -1\rangle$  hyperfine state is prepared in a crossed optical dipole trap at a magnetic field of about 5 G. The trap is positioned onto the nodal line of the radiofrequency field of a linear Paul trap. Along the axis of the Paul trap the centers of the atom and ion trap are separated by about  $300 \mu\text{m}$  to avoid unwanted atom-ion collisions (Fig. 1d). At atomic temperatures of about 700 nK and peak densities  $n_0 \approx 5 \times 10^{13} \text{ cm}^{-3}$  the total three-body recombination rate in the gas is  $\Gamma_{\text{rec}} = L_3 n_0^2 N_{\text{at}} / 3^{5/2} \approx 10 \text{ kHz}$ . Here, the three-body loss rate coefficient  $L_3$  was taken from ref<sup>3</sup>. At the rate  $\Gamma_{\text{rec}}$ , pairs of  $\text{Rb}_2$  molecules and  $\text{Rb}$  atoms are formed as final products of the reactions. Both atom and molecule would generally be lost from the shallow neutral particle trap due to the comparatively large kinetic energy they gain in the recombination event (in our case typically on the order of a few  $\text{K} \times k_B$  where  $k_B$  is the Boltzmann constant). The molecule, however, can be state-selectively ionized in a REMPI process driven by the dipole trap laser. All of these molecular ions remain trapped in the deep Paul trap and are detected with single particle sensitivity (see Methods). In each experimental run, we hold the atomic sample for a time  $\tau \approx 10 \text{ s}$ . After this time we measure the number of produced ions in the trap from which we derive (after averaging over tens of runs) the ion production rate  $\Gamma_{\text{ion}}$  normalized to a cloud atom number of  $10^6$  atoms.

As a consistency check of our assumption that  $\text{Rb}_2$  molecules are ionized in the REMPI process, we verify the production of  $\text{Rb}_2^+$  molecules. For this, we perform ion mass spectrometry in the Paul trap (see Methods). We detect primarily molecular  $\text{Rb}_2^+$  ions, a good fraction of atomic  $\text{Rb}^+$  ions but no  $\text{Rb}_3^+$  ions. Our experiments show that  $\text{Rb}^+$  ions are produced in light-assisted collisions of  $\text{Rb}_2^+$  ions with  $\text{Rb}$  atoms on timescales below a few ms. Details of this dissociation mechanism are currently under investigation and will be discussed elsewhere.

Two pathways for the production of our neutral  $\text{Rb}_2$  molecules come immediately to mind. One pathway is far-off-resonant photoassociation of two colliding  $\text{Rb}$  atoms (here with a detuning of about  $500 \text{ GHz} \times h$ ). This pathway can be ruled out using several arguments, the background of which will be discussed in more depth later. For one, we observe molecules with a parity that is incompatible with photoassociation of totally spin polarized ensembles. Furthermore, we observe a dependence of the ion production rate on light intensity that is too weak to explain photoassociation.

The second pathway is three-body recombination of  $\text{Rb}$  atoms. Indeed, by investigating the dependence of the ion production rate  $\Gamma_{\text{ion}}$  (which is normalized to a cloud atom number of  $10^6$  atoms) on atomic density, we find the expected quadratic dependence (see Fig. 2). For this measurement the density was adjusted by varying the cloud atom number while keeping the light intensity of the dipole trap constant.

Next, we investigate the dependence of the ion production rate on

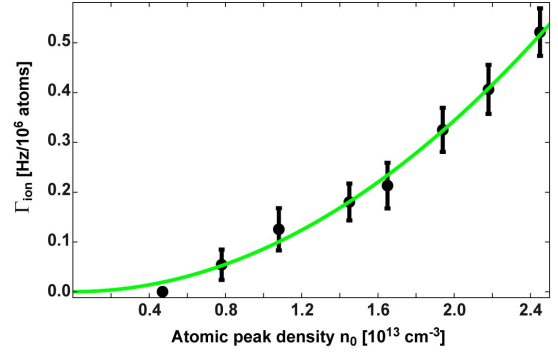


**Figure 2 | Dependence of the ion production rate  $\Gamma_{\text{ion}}$  on atomic density.  $\Gamma_{\text{ion}}$  is normalized to a cloud atom number of  $10^6$  atoms. The data are well described by a quadratic fit (solid green line). They were taken at a constant dipole trap laser intensity  $I_L = 36 \text{ kW/cm}^2$  and a laser frequency of  $\nu_L = 281630 \text{ GHz}$ .**

the wavelength of the narrow-linewidth dipole trap laser (see Methods). We scan the wavelength over a range of about 0.3 nm around 1064.5 nm, corresponding to a frequency range of about 60 GHz. Typical frequency step sizes are 50 MHz or 100 MHz. We obtain a rich spectrum of resonance lines which is shown in Fig. 3a. The quantity  $\bar{\Gamma}_{\text{ion}}$  denotes the ion production rate normalized to the atom number of the cloud and to the square of the atomic peak density. We find strongly varying resonance strengths and at first sight fairly irregular frequency spacings. In the following we will argue that most resonance lines can be attributed to respective well-defined molecular levels (resolving vibrational, rotational and often even hyperfine structure) that have been populated in the recombination process. These levels are located in the triplet or singlet ground state,  $a^3\Sigma_u^+$  and  $X^1\Sigma_g^+$ , respectively. The relatively dense distribution of these lines reflects that a fairly broad range of states is populated. A direct assignment of the observed resonances is challenging, as it hinges on the precise knowledge of the level structure of all the relevant ground and excited states. In the following we will access and understand the data step by step.

One feature of the spectrum that catches the eye is the narrow linewidth of many lines. For example, Fig. 3b shows a resonance of which the substructures have typical half-widths  $\Delta\nu_r \approx 50 \text{ MHz}$ . This allows us to roughly estimate the maximal binding energy of the molecules involved. Since the velocity of the colliding ultracold atoms is extremely low, the kinetics of the recombination products is dominated by the released molecular binding energy  $E_b$ . Due to energy and momentum conservation the molecules will be expelled from the reaction with a molecular velocity  $v_{\text{Rb}_2} = \sqrt{2E_b/(3m_{\text{Rb}_2})}$  where  $m_{\text{Rb}_2}$  is the molecular mass. The molecular resonance frequency  $\nu_0$  will then be Doppler-broadened with a half-width  $\Delta\nu_D = \sqrt{3}\nu_0 v_{\text{Rb}_2}/2c$ . Here,  $c$  is the speed of light. By comparing  $\Delta\nu_D$  to the observed values of  $\Delta\nu_r$  we estimate a maximal binding energy on the order of  $E_{b,\text{max}} \approx h \times 2.5 \text{ THz}$ . This simple analysis overestimates the value  $E_{b,\text{max}}$  since it neglects the natural linewidth of the transition and possible saturation broadening. Still, it already strongly constrains the possible populated molecular levels that are observed in our experiment.

Next, we investigate the dependence of the ion production rate on laser intensity  $I_L$ . In our experimental setup, this measurement is rather involved because the laser driving the REMPI process also confines the atomic cloud. Thus, simply changing only the laser intensity

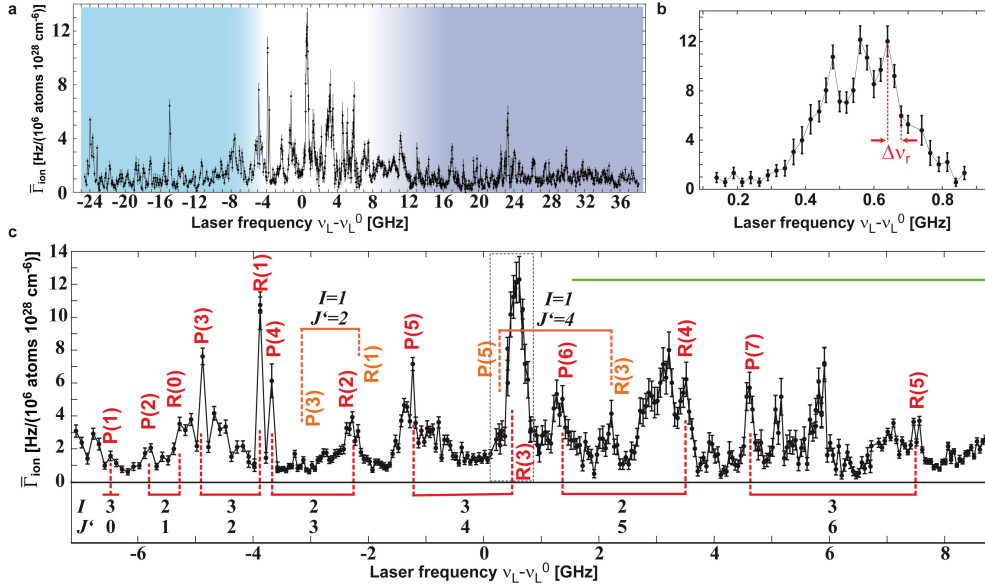


**Figure 3 | REMPI spectrum.** a, A scan of the dipole trap laser frequency  $\nu_L$  over more than 60 GHz around an offset frequency  $\nu_L^0 = 281.610$  THz shows a multitude of resonance lines. Each data point is the result of 30 to 60 repetitions of the experiment with ion detection on the single particle level. The total spectrum was obtained over a time span of 2 months. Checks of the long-term consistency of resonance positions and strengths were performed. Spectral regions dominated by transitions to  $c^3\Sigma_g^+$  are indicated by the shaded areas in dark and light blue ( $0_g^-$  and  $1_g$  component, respectively). b, High-resolution scan of the strong resonance at  $\nu_L - \nu_L^0 \approx 0.5$  GHz. c, Central spectral region with assigned P/R branches of the transition  $X^1\Sigma_g^+(v = 115) \rightarrow A^1\Sigma_u^+(v' = 68)$ . The corresponding quantum numbers  $I$  and  $J'$  are given. P(J) marks the transition  $J \rightarrow J + 1$ , R(J) the transition  $J \rightarrow J - 1$ . These lines can be grouped into pairs sharing the same  $J'$  of the excited state and  $I$  quantum number. The region where also transitions to  $b^3\Pi_u$  appear is marked by a green horizontal bar.

would undesirably also change the density  $n_0$  of the atoms. To prevent this from happening we keep  $n_0$  constant ( $n_0 \approx 5 \times 10^{13} \text{ cm}^{-3}$ ) by adjusting the atom number and temperature appropriately. Due to these experimental complications we can only vary  $I_L$  roughly by a factor of 2 (Fig. 4a). We set the laser frequency to the value of  $\nu_L = \nu_L^0 \equiv 281610$  GHz, on the tail of a large resonance (see Fig. 3). The atomic temperatures in this measurement range between 500 nK and 1.1  $\mu$ K, well above the critical temperatures for Bose-Einstein condensation. The atomic densities can therefore be described using a Maxwell-Boltzmann distribution. Assuming a simple power-law dependence of the form  $\bar{\Gamma}_{\text{ion}} \propto I_L^\alpha$  we obtain the best fit using an exponent  $\alpha = 1.5(1)$  (solid green line in Fig. 4a). This fit is between a linear and a quadratic intensity dependence (dashed red and blue lines, respectively). Thus, at least two of the three transitions composing the ionization process are partially saturated at the typical intensities used.

In order to better circumvent possible density variations of the atomic cloud induced by changes in laser intensity, we employ a further method which enables us to vary the intensity with negligible effects on the atomic sample. We achieve this by keeping the time-averaged intensity  $\langle I_L \rangle$  constant and comparing the ion production rates within a continuous dipole trap and a “chopped” dipole trap in which the intensity is rapidly switched between 0 and  $2I_L$ . In both cases the trap is operated at an intensity  $\langle I_L \rangle \approx 15 \text{ kW/cm}^2$ . In the “chopped” configuration the intensity is switched at a frequency of 100 kHz so that the atoms are exposed to the light for 5  $\mu$ s followed by 5  $\mu$ s without light. It should be noted that molecules formed in the “dark” period with sufficiently high kinetic energies may leave the central trapping region before the laser light is switched back on. They are then lost for our REMPI detection. Taking into account the molecular velocity and

the transverse extensions of the laser beams we can estimate that this potential loss mechanism leads to errors of less than 30%, even at the highest binding energies relevant to this work ( $E_b \approx h \times 750$  GHz, see below). We did not observe evidence of such losses experimentally. Investigations were made by changing the chopping frequency. We define  $R$  as ratio of the ion production rates in the “chopped” and the continuous trap configuration. Fig. 4b shows the results of these measurements for various laser frequencies  $\nu_L$ . We find a value  $R \approx 1.5$  for off-resonant frequency settings  $\nu_L - \nu_L^0 < 0.4$  GHz, in good agreement with the result presented in Fig. 4a. When scanning the laser onto resonance at  $\nu_L - \nu_L^0 \approx 0.45$  GHz (see also Fig. 3b) we obtain  $R \approx 1$ . This result indicates a linear intensity dependence of the REMPI process in the resonant case, which is explained by the saturation of two of the three molecular transitions involved. It is known that transitions into the ionization continuum (photon III, see Fig. 1e) will not saturate under the present experimental conditions. This means that the excitation pathway via photon I and II must be saturated and therefore both close to resonance.

However, given the wavelength range of about  $1064.5 \pm 0.15$  nm, an inspection of the level structure shows that photon I can only resonantly drive three different transitions which connect vibrational levels in states  $X$  and  $a$  to vibrational levels in states  $A$ ,  $b$  and  $c$  (see Fig. 1e). Spectroscopic details for these transitions and the corresponding vibrational levels are given in the Methods section and in Fig. 5. From recent spectroscopic studies<sup>27–29</sup> and additional measurements in our lab<sup>30</sup> the level structure of all relevant levels of the  $X$ ,  $a$ ,  $A$ ,  $b$ , and  $c$  states is well known. The absolute precision of most of the level energies is far better than 1 GHz for low rotational quantum numbers  $J$ .

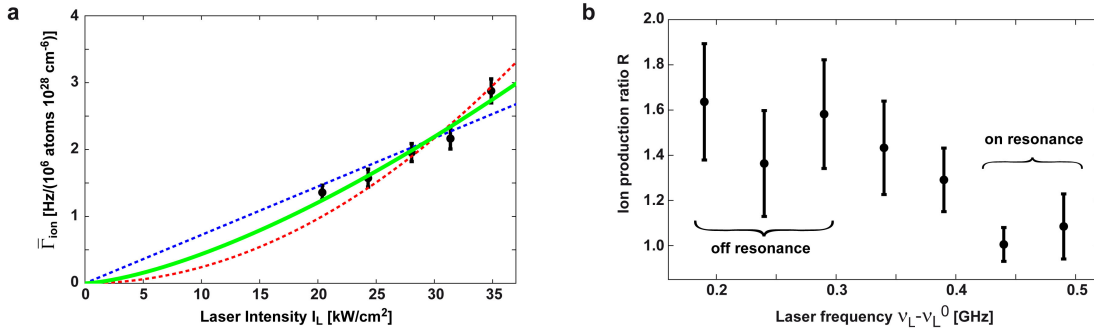


**Figure 4 | Dependence of the ion production rate on the intensity of the dipole trap laser. a,** Assuming a power-law dependence  $\bar{\Gamma}_{\text{ion}} \propto I_L^\alpha$ , the best fit to the data is achieved for  $\alpha \approx 1.5$  (solid green line). Linear and quadratic fits are also given (blue and red dashed lines, respectively). **b,** Measurement of the intensity dependence using a "chopped" dipole trap. The ratio  $R \approx 1$  on resonance indicates saturation of both transitions I and II.

In the experimental data (Fig. 3a) the central region from  $\nu_L - \nu_L^0 = -6$  to 7 GHz is marked by several prominent resonances that are significantly stronger than those observed throughout the rest of the spectrum. These resonance peaks can be explained by transitions from the  $X$  ground state to  $A$  and  $b$  states. The prominence of these singlet transitions is explained by the near degeneracy of levels due to small hyperfine splittings. Indeed, by analyzing these strong resonances with regard to line splittings and intensities it was possible to consistently assign rotational ladders for total nuclear spin quantum numbers  $I = 1, 2, 3$  for the transition  $X(v = 115) \rightarrow A(v' = 68)$ . The starting point of the rotational ladder for  $I = 2$  was fixed by previous spectroscopic measurements<sup>30</sup>. At frequencies  $\nu_L - \nu_L^0 \gtrsim 2$  GHz additional strong lines appear that we attribute to the  $X(v = 109) \rightarrow b(v' = 72)$  transition. The fact that we observe  $X$  state molecules with  $I = 1, 2, 3$  is interesting because for  $I = 1, 3$  the total parity of the molecule is negative, while for  $I = 0, 2$  it is positive. However, a two-body collision state of our spin polarized Rb atoms necessarily has positive total parity due to symmetry arguments and a photoassociation pathway would lead to ground state levels with positive parity. The observed production of molecules with negative total parity must then be a three-body collision effect.

We now consider the role of secondary atom-molecule collisions which would change the product distribution due to molecular relaxation. Two aspects are of importance: 1) depopulation of detected molecular levels and 2) population of detected molecular levels via relaxation from more weakly bound states. In our experiments reported here we detect molecules that are formed in states with binding energies on the order of hundreds of GHz. These molecules leave the reaction with kinetic energies of several  $\text{K} \times k_B$ . At these energies the rate coefficients for depopulating atom-molecule collisions are small (see e.g. ref.<sup>16</sup>) and the collision probability before the molecule is either ionized or has left the trap is below 1%.

For the population processes, we can estimate an upper bound for rate coefficients by assuming recombination to occur only into the most weakly bound state with a binding energy of  $24 \text{ MHz} \times h$ . In this case subsequent atom-molecule collision rates will be roughly comparable to those expected in the ultracold limit. At typical rate coefficients of  $10^{-10} \text{ cm}^3/\text{s}$  (see refs.<sup>31-34</sup>) and the atomic densities  $n_0 \sim 1 \times 10^{13} \text{ cm}^{-3}$  used in the measurement shown in Fig. 2, the collision probability before the molecule leaves the atom cloud is around 5%. This small probability grows linearly with density so that the density dependence of the ion production rate should show a significant

cubic contribution if secondary collisions were involved (as expected for this effective four-body process). This is inconsistent with the data and thus indicates that the population that we detect is not significantly altered by secondary collisions.

We can roughly estimate the range of molecular rotation  $J$  of the populated levels in the ground state. The strong isolated lines that we have assigned to the  $X(v = 115) \rightarrow A(v' = 68)$  transition are all contained within a relatively small spectral region ( $|\nu_L - \nu_L^0| < 6 \text{ GHz}$ ) and are explained by rotational quantum numbers  $J \leq 7$ . Population of higher rotational quantum numbers would result in a continuation of the strong resonance lines stretching to transition frequencies beyond  $\nu_L - \nu_L^0 = 10 \text{ GHz}$ , which we do not observe. Similarly, if only rotational quantum numbers  $J \leq 5$  were populated, a spectrum would result which does not have enough lines to explain the data. Thus, we can roughly set the limits on the molecular rotation to  $J \leq 7$ , a value that is also consistent with our observations of the spread of the transitions  $X \rightarrow b$  and  $a \rightarrow c$  (see Fig. 5). Finding quantum numbers as high as  $J = 7$  is remarkable because the three-body collisions at  $\mu\text{K}$  temperatures clearly take place in an  $s$ -wave regime, i.e. at vanishing rotational angular momentum. Hence, one could expect to produce  $X$  state molecules dominantly at  $J = 0$ , which, however, we do not observe.

Despite the limited spectral range covered by our measurements, we can already estimate the number of molecular vibrational levels populated in the recombination events. From the three states  $X(v = 109)$ ,  $a(v = 26)$  and  $X(v = 115)$  that we can observe within our wavelength range, all deliver comparable signals in the spectrum of Fig. 3. This suggests that at least all vibrational states more weakly bound than  $X(v = 109)$  should be populated, a total of 38 vibrational levels (counting both singlet and triplet states). This is a significant fraction of the 169 existing levels of the  $X$  and  $a$  states, although restricted to a comparatively small range of binding energies.

In conclusion, we have carried out a first, detailed experimental study of the molecular reaction products after three-body recombination of ultracold Rb atoms. We use a high-power, narrow-linewidth laser to state-selectively ionize the produced molecules in a REMPI process. Subsequently, these ions are trapped in an ion trap and detected with very high sensitivity and negligible background. An analysis of the ionization spectrum allows us to identify population of several vibrational quantum levels indicating that the recombination events result in a fairly broad and uniform population distribution. We conjecture that dozens of vibrational levels are populated in total.

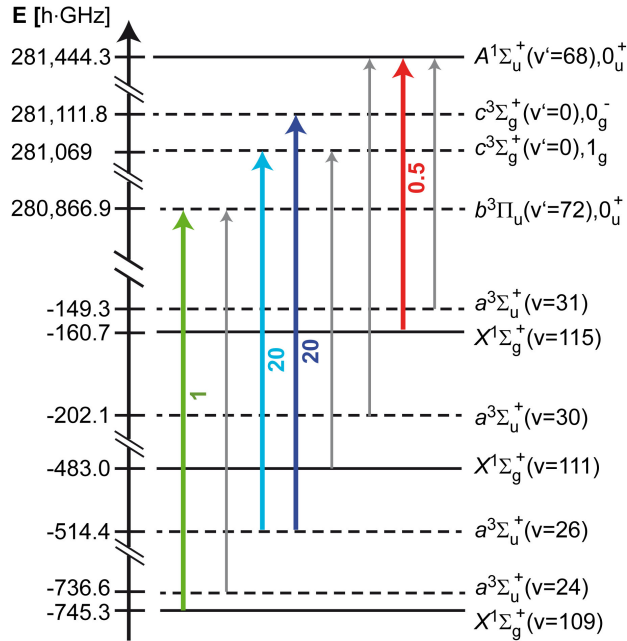


**Figure 5 | Overview over relevant molecular levels and transitions.** The vertical axis denotes the energy  $E_b$  of the energetically lowest levels of each vibrational manifold with respect to the  $5s5s$  asymptote. Colored thick arrows represent molecular transitions relevant to the spectrum of Fig. 3. The expected relative strengths of these transitions are also given. Grey arrows mark transitions that occur in the relevant spectral region but are so weak that they can be neglected (for further spectroscopic details see Methods). We identify three main molecular transitions for the initial step of the REMPI process. (1) Molecules in the  $v = 26$  vibrational level of the  $a^3\Sigma_u^+$  potential are excited to the  $v' = 0$  level of the  $c^3\Sigma_g^+$  potential. This level is split into a  $1_g$  and a  $0_g^-$  component. (2) Excitation from  $X^1\Sigma_g^+(v = 115)$  to  $A^1\Sigma_u^+(v' = 68)$ . (3) Excitation from  $X^1\Sigma_g^+(v = 109)$  to  $b^3\Pi_u(v' = 72)$ . Transition (3) becomes possible through the strong spin-orbit coupling of the  $A$  and  $b$  states.

Molecules are produced both in  $X^1\Sigma_g^+$  as well as  $a^3\Sigma_u^+$ , with negative and positive total parity, various total nuclear spins and rotational quantum numbers reaching  $J \leq 7$ . Our work represents a first experimental step towards a detailed understanding on how the reaction channels in three-body recombination are populated. A full understanding will clearly require further experimental and theoretical efforts. On the experimental side the scanning range has to be increased and it could be advantageous to switch to a two-color REMPI scheme in the future. Such studies may finally pave the way to a comprehensive understanding of three-body recombination, which includes the details of the final products.

Reaching beyond the scope of three-body recombination, the great sensitivity of our detection scheme has enabled us to state-selectively probe single molecules that are produced at rates of only a few Hz. We thereby demonstrate a novel scheme for precision molecular spectroscopy in extremely dilute ensembles.

## METHODS

**Dipole trap and REMPI configuration.** The crossed dipole trap is composed of a horizontal and a vertical beam focussed to beam waists of  $\sim 90 \mu\text{m}$  and  $\sim 150 \mu\text{m}$ , respectively. It is positioned onto the nodal line

of the radiofrequency field of the linear Paul trap with  $\mu\text{m}$  precision. The two trap centers are separated by about  $300 \mu\text{m}$  along the axis of the Paul trap (see Fig. 1d). In a typical configuration, the trap frequencies of the dipole trap are  $(175, 230, 80)$  Hz resulting in atom cloud radii of about  $(6, 7, 16) \mu\text{m}$ . The short-term frequency stability of the dipole trap laser source is on the order of 1 kHz and it is stabilized against thermal drifts to achieve long-term stability of a few MHz. The two beams of the dipole trap are mutually detuned by 160 MHz to avoid interference effects in the optical trap. Consequently, two frequencies are in principle available to drive the REMPI process. However, the intensity of the horizontal beam is 4 times larger than the one of the vertical beam and we have not directly observed a corresponding doubling of lines. Further details on the atom-ion apparatus are given in ref<sup>35</sup>.

**Paul trap configuration.** The linear Paul trap is driven at a radiofrequency of 4.17 MHz and an amplitude of about 500 V resulting in radial confinement with trap frequencies of  $(\omega_{x,\text{Ba}}, \omega_{y,\text{Ba}}) = 2\pi \times (220, 230)$  kHz for a  $^{138}\text{Ba}^+$  ion. Axial confinement is achieved by applying static voltages to two endcap electrodes yielding  $\omega_{z,\text{Ba}} = 2\pi \times 40.2$  kHz. The trap frequencies for "dark"  $\text{Rb}_2^+$  and  $\text{Rb}^+$  ions produced in the REMPI processes are  $(m_{\text{Ba}}/m_{\text{dark}} \times \omega_{x,\text{Ba}}, m_{\text{Ba}}/m_{\text{dark}} \times \omega_{y,\text{Ba}}, \sqrt{m_{\text{Ba}}/m_{\text{dark}}} \times \omega_{z,\text{Ba}})$  where  $m_{\text{Ba}}$  and  $m_{\text{dark}}$  denote the mass of the  $\text{Ba}^+$  ion and the dark ion, respectively. The depth of the Paul trap depends on the ionic mass and exceeds 2 eV for all ionic species relevant to this work.

**Ion detection methods.** We employ two methods to detect  $\text{Rb}_2^+$  and  $\text{Rb}^+$  ions both of which are not amenable to fluorescence detection. In the first of these methods we use a single trapped and laser-cooled  $^{138}\text{Ba}^+$  ion as a probe. By recording its position and trapping frequencies in small ion strings with up to 4 ions we detect both the number and the masses of the ions following each REMPI process (see also<sup>36</sup>). The second method is based on measuring the number of ions in the Paul trap by immersing them into an atom cloud and recording the ion-induced atom loss after a hold time of 2 s (see also<sup>37</sup>). During this detection scheme, we take care to suppress further generation of ions by working with small and dilute atomic clouds and by detuning the REMPI laser from resonance. Both methods are background-free in the sense that no ions are captured on timescales of days in the absence of the atom cloud. Further information on both detection methods is given in the Supplementary Information.

**Spectroscopic details.** Spin-orbit and effective spin-spin coupling in the  $A$ ,  $b$ , and  $c$  states lead to Hund's case c coupling where the relevant levels of states  $A$  and  $b$  have  $0_u$  symmetry while the levels of state  $c^3\Sigma_g^+$  are grouped into  $0_g^-$  and  $1_g$  components. The level structure of the  $0_u^+$  states is quite simple as it is dominated by rotational splittings. Typical rotational constants for the electronically excited states are on the order of 400 MHz, for the weakly bound  $X$  and  $a$  states they are around 100-150 MHz.

Figure 5 shows the relevant optical transitions between the  $X$ ,  $a$  states and the  $A$ ,  $b$ ,  $c$  states in our experiment. For the given expected relative strengths of these transitions, we only consider Franck-Condon factors and the mixing of singlet and triplet states, while electronic transition moments are ignored. The colored arrows correspond to transitions with large enough Franck-Condon factors (typ.  $10^{-2} \dots 10^{-3}$ ) so that at laser powers of  $\approx 10^4$  W/cm<sup>2</sup> resonant transitions can be well saturated. Transitions marked with grey arrows can be neglected due to weak transition strengths, resulting from small Franck-Condon factors or dipole selection rules.

The authors would like to thank Stefan Schmid and Andreas Brunner for support during early stages of the experiment and Olivier Dulieu, Brett Esry, Jose d'Incao, William Stwalley, Ulrich Heinzmann, Jeremy Hutson, Pavel Soldan, Thomas Bergeman and Anastasia Drozdova for valuable information and fruitful discussions. This work was supported by the German Research Foundation DFG within the SFB/TRR21.

1. Hess, H. F. *et al.* Observation of three-body recombination in spin-polarized Hydrogen. *Phys. Rev. Lett.* **51**, 483–486 (1983).
2. Burt, E. A. *et al.* Coherence, correlations, and collisions: What one learns about Bose-Einstein condensates from their decay. *Phys. Rev. Lett.* **79**, 337–340 (1997).
3. Söding, J. *et al.* Three-body decay of a Rubidium Bose-Einstein condensate. *Applied Physics B* **69**, 257–261 (1999).
4. Esry, B. D., Greene, C. H. & Burke, J. P. Recombination of three atoms in the ultracold limit. *Phys. Rev. Lett.* **83**, 1751–1754 (1999).
5. Suno, H. & Esry, B. D. Three-body recombination in cold helium-helium-alkali-metal-atom collisions. *Phys. Rev. A* **80**, 062702 (2009).
6. Wang, Y., D'Incao, J. P. & Esry, B. D. Cold three-body collisions in hydrogen-hydrogen-alkali-metal atomic systems. *Phys. Rev. A* **83**, 032703 (2011).
7. Guevara, N. L., Wang, Y. & Esry, B. D. New Class of Three-Body States. *Phys. Rev. Lett.* **108**, 213202 (2012).
8. Fedichev, P. O., Reynolds, M. W. & Shlyapnikov, G. V. Three-body recombination of ultracold atoms to a weakly bound  $s$  level. *Phys. Rev. Lett.* **77**, 2921–2924 (1996).
9. Bedaque, P. F., Braaten, E. & Hammer, H.-W. Three-body recombination in Bose gases with large scattering length. *Phys. Rev. Lett.* **85**, 908–911 (2000).
10. Efimov, V. Energy levels arising from resonant two-body forces in a three-body system. *Physics Letters B* **33**, 563 – 564 (1970).
11. Braaten, E. & Hammer, H.-W. Three-body recombination into deep bound states in a Bose gas with large scattering length. *Phys. Rev. Lett.* **87**, 160407 (2001).
12. Kraemer, T. *et al.* Evidence for Efimov quantum states in an ultracold gas of Caesium atoms. *Nature* **440**, 315–318 (2006).
13. Weber, T., Herbig, J., Mark, M., Nägerl, H.-C. & Grimm, R. Three-Body Recombination at Large Scattering Lengths in an Ultracold Atomic Gas. *Phys. Rev. Lett.* **91**, 123201 (2003).
14. Jochim, S. *et al.* Pure Gas of Optically Trapped Molecules Created from Fermionic Atoms. *Phys. Rev. Lett.* **91**, 240402 (2003).
15. d'Incao, J. private communication (2013).
16. Simoni, A. & Launay, J.-M. Ultracold atom-molecule collisions with hyperfine coupling. *Laser Physics* **16**, 707–712 (2006).
17. Bates, D. R., Kingston, A. E. & McWhirter, R. W. P. Recombination between electrons and atomic ions. I. Optically thin plasmas. *Proceedings of the Royal Society of London. Series A. Mathematical and Physical Sciences* **267**, 297–312 (1962).
18. Flower, D. R. & Harris, G. J. Three-body recombination of hydrogen during primordial star formation. *Monthly Notices of the Royal Astronomical Society* **377**, 705–710 (2007).
19. Lozeille, J. *et al.* Detection by two-photon ionization and magnetic trapping of cold  $\text{Rb}_2$  triplet state molecules. *Eur. Phys. J. D* **39**, 261–269 (2006).
20. Aymar, M., Azizi, S. & Dulieu, O. Model-potential calculations for ground and excited  $\Sigma$  states of  $\text{Rb}_2^+$ ,  $\text{Cs}_2^+$  and  $\text{RbCs}^+$  ions. *J. Phys. B: At. Mol. Opt. Phys.* **36**, 4799 (2003).
21. Fioretti, A. *et al.* Formation of Cold  $\text{Cs}_2$  Molecules through Photoassociation. *Phys. Rev. Lett.* **80**, 4402–4405 (1998).
22. Gabbanini, C., Fioretti, A., Lucchesini, A., Gozzini, S. & Mazzoni, M. Cold Rubidium Molecules Formed in a Magneto-Optical Trap. *Phys. Rev. Lett.* **84**, 2814–2817 (2000).
23. Huang, Y. *et al.* Formation, detection and spectroscopy of ultracold  $\text{Rb}_2$  in the ground  $X^1\Sigma_g^+$  state. *Journal of Physics B: Atomic, Molecular and Optical Physics* **39**, S857 (2006).
24. Salzmann, W. *et al.* Coherent transients in the femtosecond photoassociation of ultracold molecules. *Phys. Rev. Lett.* **100**, 233003 (2008).
25. Sullivan, S. T. *et al.* Trapping molecular ions formed via photoassociative ionization of ultracold atoms. *Phys. Chem. Chem. Phys.* **13**, 18859–18863 (2011).
26. Mudrich, M. *et al.* Spectroscopy of triplet states of  $\text{Rb}_2$  by femtosecond pump-probe photoionization of doped helium nanodroplets. *Phys. Rev. A* **80**, 042512 (2009).
27. Strauss, C. *et al.* Hyperfine, rotational, and vibrational structure of the  $a^3\Sigma_u^+$  state of  $^{87}\text{Rb}_2$ . *Phys. Rev. A* **82**, 052514 (2010).
28. Takekoshi, T. *et al.* Hyperfine, rotational, and Zeeman structure of the lowest vibrational levels of the  $^{87}\text{Rb}_2(1)^3\Sigma_g^+$  state. *Phys. Rev. A* **83**, 062504 (2011).
29. Drozdova, A. Ph.D. thesis, Université de Lyon and Lomonosov State University (2012).
30. To be published.
31. Mukaiyama, T., Abo-Shaeer, J. R., Xu, K., Chin, J. K. & Ketterle, W. Dissociation and Decay of Ultracold Sodium Molecules. *Phys. Rev. Lett.* **92**, 180402 (2004).
32. Staunum, P., Kraft, S. D., Lange, J., Wester, R. & Weidemüller, M. Experimental Investigation of Ultracold Atom-Molecule Collisions. *Phys. Rev. Lett.* **96**, 023201 (2006).
33. Zahzam, N., Vogt, T., Mudrich, M., Comparat, D. & Pillet, P. Atom-Molecule Collisions in an Optically Trapped Gas. *Phys. Rev. Lett.* **96**, 023202 (2006).
34. Quémener, G., Launay, J.-M. & Honvault, P. Ultracold collisions between Li atoms and  $\text{Li}_2$  diatoms in high vibrational states. *Phys. Rev. A* **75**, 050701 (2007).
35. Schmid, S., Härter, A., Frisch, A., Hoinka, S. & Hecker Denschlag, J. An apparatus for immersing trapped ions into an ultracold gas of neutral atoms. *Rev. Sci. Instrum.* **83**, 053108 (2012).
36. Schmid, S., Härter, A. & Hecker Denschlag, J. Dynamics of a Cold Trapped Ion in a Bose-Einstein Condensate. *Phys. Rev. Lett.* **105**, 133202 (2010).
37. Härter, A. *et al.* Single Ion as a Three-Body Reaction Center in an Ultracold Atomic Gas. *Phys. Rev. Lett.* **109**, 123201 (2012).
38. Morigi, G. & Walther, H. Two-species Coulomb chains for quantum information. *Eur. Phys. J. D* **13**, 261–269 (2001).
39. Berkeland, D. J., Miller, J. D., Bergquist, J. C., Itano, W. M. & Wineland, D. J. Minimization of ion micromotion in a Paul trap. *Journal of Applied Physics* **83**, 5025–5033 (1998).

# Supplementary Information

In this Supplementary Information we describe two methods that we employ to detect small numbers of  $\text{Rb}_2^+$  and  $\text{Rb}^+$  ions in our linear Paul trap.

## Method 1

To implement our first ion detection method allowing mass-sensitive detection of "dark" ions we rely on the presence of a single "bright" ion in the trap. Information on additional ions can be extracted from its fluorescence position. When using this method, our experimental procedure begins with the loading of a single  $^{138}\text{Ba}^+$ -ion into our linear Paul trap. We laser-cool the ion and image its fluorescence light onto an electron-multiplying charge-coupled device camera. This enables us to determine the position of the trap center to better than 100 nm. The ion is confined at radial and axial trapping frequencies  $\omega_{r,\text{Ba}} \approx 2\pi \times 220$  kHz and  $\omega_{\text{ax},\text{Ba}} \approx 2\pi \times 40.2$  kHz and typically remains trapped on timescales of days. Next, we prepare an ultracold atomic sample in the crossed dipole trap. At typical atomic temperatures of about 700 nK the atom cloud has radial and axial extensions of about  $7 \mu\text{m}$  and  $15 \mu\text{m}$  and is thus much smaller than the trapping volume of our Paul trap. To avoid atom-ion collisions we shift the  $\text{Ba}^+$ -ion by about  $300 \mu\text{m}$  with respect to the atom cloud before the atomic sample arrives in the Paul trap. The shifting is performed along the axis of the trap by lowering the voltage on one of the endcap electrodes. Additionally, we completely extinguish all resonant laser light so that the atoms are only subjected to the light of the dipole trap. The atomic sample is moved into the center of the radial trapping potential of the Paul trap and is typically held at this position for a time  $\tau_{\text{hold}} \approx 10$  s. Despite the axial offset from the center of the Paul trap, the atom cloud at this position is fully localized within the trapping volume of the Paul trap. After the hold time the sample is detected using absorption imaging. Subsequently, the ion cooling beams are switched back on for fluorescence detection of the  $\text{Ba}^+$ -ion.

The presence of a second ion in the trap leads to positional shifts of the  $^{138}\text{Ba}^+$ -ion by distances on the order of  $10 \mu\text{m}$  (see Fig. 1). We make use of the mass-dependent trap frequencies of the Paul trap to gain information on the ion species trapped. In a two-ion Coulomb crystal composed of a  $\text{Ba}^+$ -ion and a dark ion, the axial center-of-mass frequency  $\omega_{\text{ax},2\text{ion}}$  shifts with respect to  $\omega_{\text{ax},\text{Ba}}$  depending on the mass of the dark ion  $m_{\text{dark}}$ <sup>38</sup>. We measure  $\omega_{\text{ax},2\text{ion}}$  by modulating the trap drive at frequencies  $\omega_{\text{mod}}$  and by monitoring the induced axial oscillation of the  $\text{Ba}^+$ -ion, visible as a blurring of the fluorescence signal. In this way, after each ion trapping event, we identify a resonance either at  $\omega_{\text{mod}} \approx 2\pi \times 44$  kHz or  $\omega_{\text{mod}} \approx 2\pi \times 38$  kHz corresponding to  $m_{\text{dark}} = 87\text{u}$  and  $m_{\text{dark}} = 174\text{u}$ , respectively (see table 1).

We have expanded this method for ion strings with up to four ions including the  $\text{Ba}^+$ -ion. For this purpose, we perform the following step-by-step analysis.

1. The position  $x$  of the  $\text{Ba}^+$ -ion with respect to the trap center is detected. If  $x \neq 0$ , the value of  $x$  allows us to directly determine the total number of ions in the string.
2. If  $x = 0$  we need to distinguish between a single  $\text{Ba}^+$  ion and a

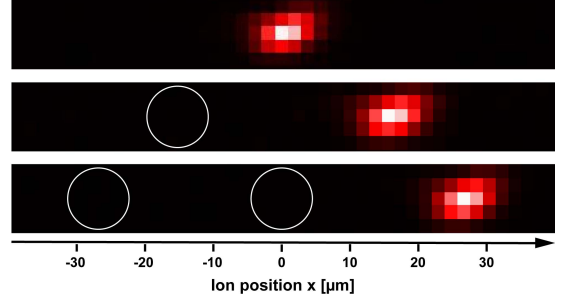


**Figure 1 | Ion detection using a  $^{138}\text{Ba}^+$ -ion.** Positional shifts of the fluorescence of the  $\text{Ba}^+$ -ion and measurements of the trap oscillation frequencies allow us to perform mass-sensitive detection of up to three "dark" ions in the trap.

**Table 1 | Trap oscillation frequencies of two-ion crystals**

Ion species	$\omega_{\text{ax},2\text{ion}}/2\pi$ [kHz]	$\omega_r/2\pi$ [kHz]
$^{138}\text{Ba}^+$ and $^{138}\text{Ba}^+$	40.2	220.0
$^{138}\text{Ba}^+$ and $^{87}\text{Rb}^+$	44.0	345.3
$^{138}\text{Ba}^+$ and $^{87}\text{Rb}_2^+$	37.7	170.7

three-ion string with  $\text{Ba}^+$  at its center. This is done by modulating the trap drive at  $\omega_{\text{ax},\text{Ba}}$ , thereby only exciting the  $\text{Ba}^+$  ion if no further ions are present.

3. We destructively detect the  $\text{Rb}^+$  ions by modulating the trap drive on a 5 kHz wide band around  $2 \times \omega_{r,\text{Rb}}/(2\pi) = 691$  kHz. This selectively removes only  $\text{Rb}^+$  ions from the string making use of the relatively weak inter-ionic coupling when exciting the ions radially.
4. Steps 1. and 2. are repeated to detect the number of remaining ions.
5. The  $\text{Rb}_2^+$  ions are destructively detected via modulation around  $2 \times \omega_{r,\text{Rb}2}/(2\pi) = 341$  kHz.

## Method 2

We have also developed a second ion detection method that does not require an ion fluorescence signal. Instead, the trapped ions are detected via their interaction with an atomic sample. For this purpose, we produce a comparatively small atom cloud containing about  $1 \times 10^5$  atoms at a density of a few  $10^{12} \text{ cm}^{-3}$ . In addition, we set the frequency of the dipole trap laser to an off-resonant value so that the production of additional ions during the ion probing procedure becomes extremely unlikely. We now fully overlap the ion and atom traps for an interaction time  $\tau_{\text{int}} = 2$  s. By applying an external electric field of several V/m we set the ion excess micromotion energy to values on the order of tens of  $k_B \times \text{mK}$ <sup>37,39</sup>. Consequently, if ions are present in the trap, strong atom losses occur due to elastic atom-ion collisions. Fig.2 shows a histogram of the atom numbers of the probe atom samples consisting of the outcome of about 1,000 experimental runs. The histogram displays several peaks which can be assigned to the discrete

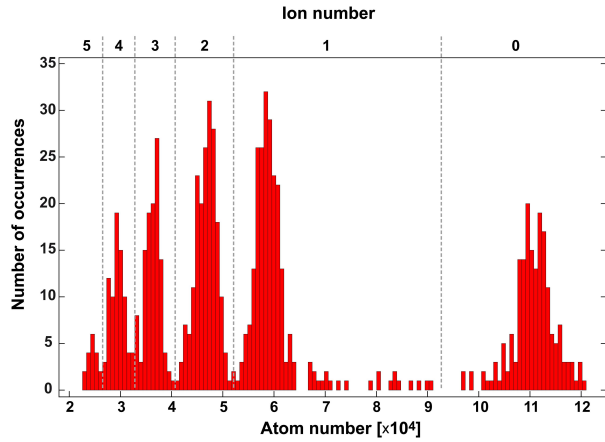


**Figure 2 | Ion detection method based on ion-induced atom loss.**

We overlap an ultracold atom cloud containing approximately 110,000 atoms with the center of the Paul trap. After an interaction time  $\tau = 2$  s we detect the ion-induced atom loss via absorption imaging of the atom cloud. The discrete number of trapped ions is clearly reflected in the displayed histogram of atom numbers.

number of ions in the trap. Up to five ions were trapped simultaneously and detected with high fidelity. The atom loss rate increases nonlinearly with ion number mainly because the interionic repulsion prevents the ions from all occupying the trap center where the atomic density is maximal. While ion detection method 2 does not distinguish ionic masses, it has advantages in terms of experimental stability and does not require the trapping of ions amenable to laser cooling or other fluorescence based detection techniques.